

Article

Distribution and Genesis of the Deep Buried, Fractured and Vuggy Dolostone Reservoir in the Lower Ordovician Succession, North Tarim Basin, Northwestern China

Lijun Gao ^{1,2}, Jie Li ^{3,*} , Guorong Li ⁴, Liyun Fu ¹  and Yongli Liu ²

¹ National Key Laboratory of Deep Oil and Gas, China University of Petroleum (East China), Qingdao 266580, China

² Sinopec Northwest Oil Field Company, Urumqi 841100, China

³ Hubei Key Laboratory of Oil and Gas Exploration and Development in Hubei Province and Key laboratory of Tectonics and Petroleum Resources, China University of Geosciences, Wuhan 430074, China

⁴ College of Energy, Chengdu University of Technology, Chengdu 610500, China

* Correspondence: lijie@cug.edu.cn

Abstract: Recently, a series of prolific fracture-vug reservoirs have been discovered in the lower Ordovician dolostone successions of the northern Tarim Basin. However, the genesis of these reservoirs remains unclear. In this study, observations on drilling cores and thin sections identify the pore space characterized by dissolved fractures, fissures, and vugs. Petrology, cathodoluminescence, and homogenization temperatures of fluid inclusions aid in establishing the diagenetic paragenetic sequence. Dissolving enlargement occurred after chemical compaction of overlying limestone and before the Permian volcanic activity. Breccia pores containing unique fillings of terrestrial materials (quartz sand and allogenic kaolinite) and calcite cements with negative $\delta^{18}\text{O}_{\text{PDB}}$ values (-18.4%) along with $^{87}\text{Sr}/^{86}\text{Sr}$ ratios (up to 0.71026) indicate that the dissolving fluid originated from meteoric freshwater at the surface. The $\delta^{18}\text{O}_{\text{SMOW}}$ values of the calcite precipitating fluid (-2.1% to -8.7%) further suggest freshwater as the source of the dissolving fluid, buffered by the Ordovician wall rocks or formation water. As the distance from the unconformity surface increases, both the homogenization temperature and $\delta^{18}\text{O}_{\text{PDB}}$ values of the breccia pore-filling calcite in the southern study area gradually elevate and deplete, respectively, indicating a rise in temperature during the infiltration of meteoric freshwater with increasing subsurface temperatures. The abnormal reflection bodies identified as reservoirs in seismic profiles along deep-seated strike-slip faults delineate these faults as the channel for the infiltration of meteoric freshwater. The penetrating strata of these faults and the high $^{87}\text{Sr}/^{86}\text{Sr}$ values of breccia pore-filling calcite suggest that karstification occurred during the Devonian period. Accordingly, we establish a deep karst model in which the Devonian meteoric freshwater penetrated along the strike-slip faults and dissolved the Ordovician dolostones, resulting in the development of deep buried karstic fault reservoirs in the southern region of the northern Tarim Basin.

Keywords: meteoric freshwater; deep karst; dissolved stylolite; negative oxygen isotopes; strontium isotopes; dissolving enlargement; breccia pore-filling; strike slip fault; Yingshan Formation



Citation: Gao, L.; Li, J.; Li, G.; Fu, L.; Liu, Y. Distribution and Genesis of the Deep Buried, Fractured and Vuggy Dolostone Reservoir in the Lower Ordovician Succession, North Tarim Basin, Northwestern China. *Minerals* **2024**, *14*, 58. <https://doi.org/10.3390/min14010058>

Academic Editor: Ricardo Ferreira Louro Silva

Received: 23 November 2023

Revised: 16 December 2023

Accepted: 20 December 2023

Published: 2 January 2024



Copyright: © 2024 by the authors. Licensee MDPI, Basel, Switzerland. This article is an open access article distributed under the terms and conditions of the Creative Commons Attribution (CC BY) license (<https://creativecommons.org/licenses/by/4.0/>).

1. Introduction

Large-scale development of dissolved fractures and vugs in carbonate successions beneath unconformities are generally karst products during subaerial exposure, and several classic epigenetic karst models have been extensively used to explain the distribution and genesis of these vugs and fractures [1–3]. The genesis of dissolved fractures and vugs deep under unconformities or in even unexposed areas may be varied. In some cases, meteoric water flows along underground preexisting permeable layers and dissolves carbonate surrounding rocks driven by a hydraulic head difference, forming vug and fracture systems underground in unexposed areas [4–8]. Some other cases documented

that the underground unsaturated fluid flowed and dissolved along permeable layers or open fractures [9–12]. The distribution of dissolved fractures and vugs is distinct between different sources of fluids and hydrological frameworks, which is vital to the evaluation of underground conditions in resources, energy, hydropower, and tunnel engineering.

Since 1980s, the geologic theory of epigenetic karst has guided the discovery of large oilfields in northern Tarim Basin, such as the Tahe, Lunnan, and Halahatang oilfields. The early productive layer of these fields was the karstic limestone interval within 150 m beneath the extensive unconformity of the Middle Ordovician strata having produced 6 million tons of oil per year [13–15]. The unconformity is a counterpart to the Sauk III unconformity of the Middle Ordovician in the North America [16]. Until 2014, a series of vug-fracture reservoirs with a vertical distance of 160–400 m from the unconformity were discovered in the Lower Ordovician dolostones in the Tahe Oilfield, and then it was found that this kind of reservoir also developed extensively at depth of more than 6000 m in the southern areas of the northern Tarim Basin.

Due to the potential for energy production, its genesis and distribution has been receiving increasing attention. Some studies have suggested that the development of these dissolved fractures and vugs resulted from the lateral flow of meteoric water flowing from surface of exposed areas into the underground of unexposed areas driven by the hydraulic head difference, circulating through and dissolving the Lower Ordovician dolostones. However, the study area experienced multiple stages of tectonic uplift and subaerial exposure from the Middle Ordovician to Late Devonian period, and there is still divergence about the specific time of the meteoric-water dissolution [17,18]. Based on the geochemistry of vug fillings and the intimate relationship between reservoir distribution and faults, some studies indicated that dissolved fractures and vugs were resulted from hydrothermal fluid dissolution [19,20].

The aims of this paper are to (i) investigate the pore space type in the dolostone reservoirs, (ii) unravel the source of dissolving fluid responsible for the pore space generation, (iii) look into the distribution of the deep buried reservoirs and its relationship with unconformities and faults, and (iv) establish the geologic model of the reservoir development.

2. Geological Settings

2.1. Geography and Location

The Tarim Basin is the largest inland basin in China, with an irregular diamond shape, located between the Tianshan Mountains and the Kunlun Mountains. It has an area of more than 400,000 km² and is about 520 km wide from north to south and 1200 km wide from east to west. There are seven principal structural units, including the Kuqa Depression, Northern Depression, Central Uplift, Tabei Uplift, Southeastern Depression, Tanan Uplift and Southwest Depression [21,22]. The Northern Depression can be subdivided into the eastern Manjar Depression, the central Aman Slope and the Western Awati Depression (Figure 1A).

The Tabei Uplift is located in the northern Tarim Basin, between the Northern Depression and Kuqa Depression, striking near the east-west and leaning slightly to the north. It is 440 km wide from east to west and 80 km wide from north to south. Based on stratigraphy and structural patterns, the Tabei Uplift can be divided into six secondary structural units: the Shaxi Arch, Shaya-Luntai fault Arch, Halahatang Sag, Akkule Arch, Caohu Sag and Korle Nosing Arch (Figure 1B) [23]. Among them, the Halahatang Sag and Akkule Rise are the richest in oil and gas and the most drilling and seismic data in the Tarim Basin, which is the target area of this study (Figure 1B).

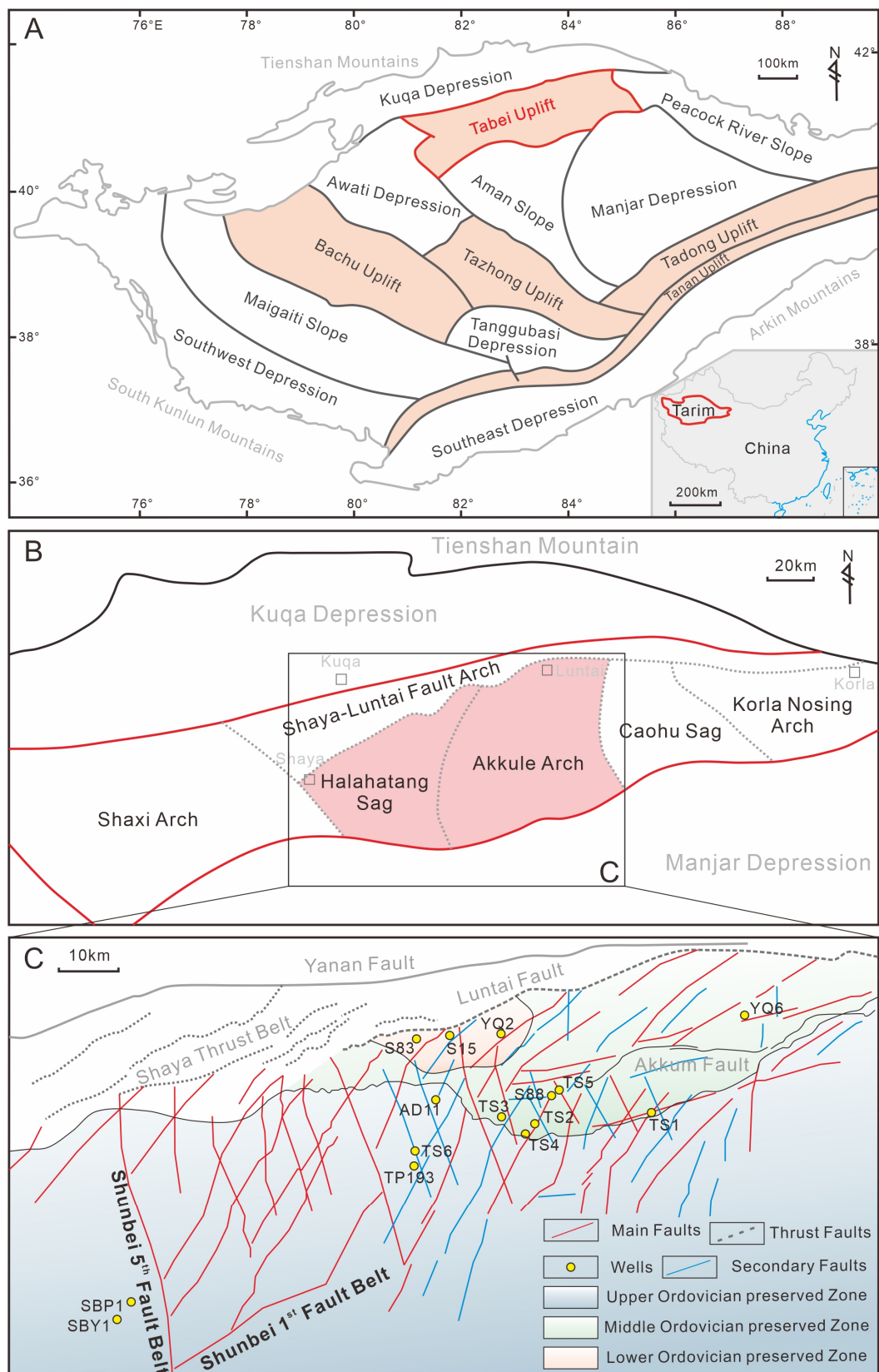


Figure 1. General maps and location of study area. **(A)** Geological settings and tectonic sections of Tarim Basin. **(B)** Subsections of the Tabei Uplift, of which the Akkule Arch and Halahatang Sag are the main study area. **(C)** Locations of study wells and their distribution in the framework of the pinchout boundary of Ordovician successions and the X-shape strike-slip faults.

2.2. Tectonics and Unconformity

The tectonic evolution of the Tabei Uplift has four stages: Firstly, the Tarim Basin possessed its basement as the result of the amalgamation of the North and South Tarim blocks during the Proterozoic period. Secondly, the northern Tarim area experienced a stable and slow uplift and denudation stage from the Middle Caledonian to the Early Hercynian period. Then during the late Hercynian to the Indo-China period, the northern Tarim area experienced compression and uplift again. Finally slight tectonic adjustment occurred from the Yanshanian to the Himalayan period [22,24].

The Ordovician strata experienced multiple stages of tectonic movements in the Paleozoic era, resulting in several unconformities. During the middle Caledonian period (Late Ordovician), the South Kunlun Ocean collided with the southern Tarim block, resulting in a tectonic uplift of the Tarim block after the deposition of the Yijianfang formation (O_{2y}) and the Lianglitag formation (O_{3l}). The northern Tarim area is far away from the collision belt and the extent of uplift is limited, forming parallel unconformities in the northern Tarim area. After the deposition of the Sangtamu formation (O_{3s}), the southern Tianshan Ocean began to subduct to the northern margin of the Tarim, and the northern Tarim block was uplifted and subaerially exposed, as a result of which the top of the Ordovician strata was denuded and partially covered by the Lower Silurian sandstone and mudstone with angular unconformity. During the middle Devonian period, the Tarim block collided with the Middle Tianshan island arc, and the Ordovician strata in the northern Tarim area was regionally exposed again and covered by Upper Devonian sandstone with angular unconformity [24–27].

The Early Hercynian epoch is key for the development of Paleozoic structural morphology, it caused not only Silurian-Upper Ordovician denudation on the surface, but also a series of deep-seated strike-slip faults [28]. The wells S88, TS1, TS2, TS3, TS4, TS5, YQ2 and YQ6, which are related to the deep Ordovician in the area, are located on the first-order strike-slip fault zone, while AD11, TS6 and TP193 are located on the secondary strike-slip fault zone (Figure 1C).

2.3. Stratigraphy

The lower Paleozoic strata in the Tabei Uplift are marine deposits, the Middle Cambrian features thick gypsum-salt rocks depositing on an evaporative platform, the Upper Cambrian and Lower Ordovician are mainly dolostones, and the Middle-Upper Ordovician is mainly limestone. During the Silurian and Devonian eras, the Tabei Uplift was uplifted to the surface, and the strata are continental sediments. The Lower Silurian (S_1) consist of interbedded sandstone and mudstone in the Kepingtag Formation and Tatartag Formation, and the Upper Devonian Donghetang Formation (D_{2d}) is porous sandstone. In the late Paleozoic, the Tabei Uplift turned into a shelf-margin sedimentary environment, and the Lower Carboniferous (C_1) is mainly interlayers of bioclastic limestone and mudstone.

The complete Ordovician stratigraphic sequence in the Tarim Basin mainly consists of the Lower Ordovician Penglaiba Formation (O_{1p}) and lower part of the Yingshan Formation (O_{1-2y^1}), the Middle Ordovician upper Yingshan Formation (O_{1-2y^2}), the Yijianfang Formation (O_{2y}), the Upper Ordovician Qiarbak Formation (O_{3q}), the Lianglitag Formation (O_{3l}), and the Sangtamu Formation (O_{3s}) from bottom to top. Among them, the dolostones in the O_{1p} and O_{1-2y^1} are the key strata in this study. Affected by the subduction of the oceanic crust on the northern side of the Tarim block, the Middle-Upper Ordovician is missing in the north of the Tabei Uplift due to tectonic uplift, while the Lower Ordovician remains (Figure 2).

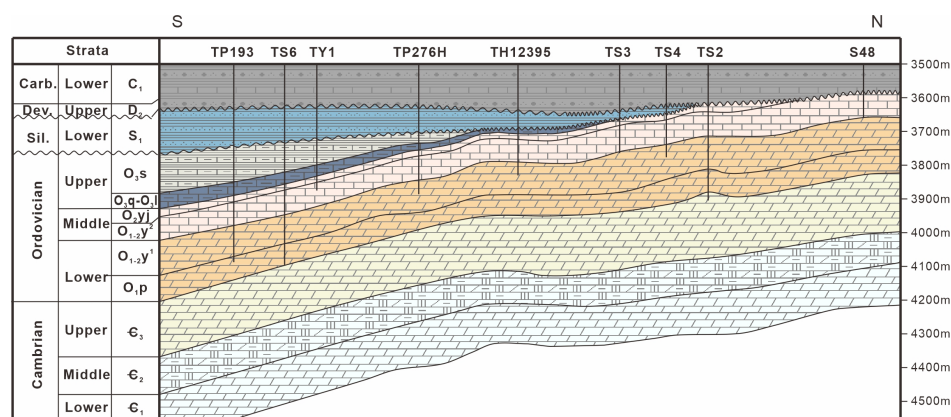


Figure 2. Paleozoic stratigraphic framework of the study area, northern Tarim Basin. Abbreviations: Carb. = Carboniferous, Dev. = Devonian, Sil. = Silurian, O_{3s} = Sangtamu Formation, O_{3l} = Lianglitag Formation, O_{3q} = Qiarbak Formation, O_{2yj} = Yijianfang Formation, O_{1-2y}¹ = the lower Yingshan Formation, O_{1-2y}² = the upper Yingshan Formation, O_{1p} = Penglaiba Formation. The wells were projected on the profile with the horizontal distance between wells not to scale.

3. Methods

The Ordovician drilling cores of 15 wells in the Tabei area were observed, and the pore space of the reservoir intervals consisted of mainly voids and dissolved fractures. Diageneses associated with karst features were examined and 209 typical samples were collected. In order to analyze the genesis and formation time of cavities and karst fractures, this study first observed the petrological characteristics of voids and karst fractures, combined with cathodoluminescence and inclusion temperature measurements to sort out the diagenetic sequence of the target layer. Based on the diagenetic sequence, the forming environments and times of typical diagenetic products were analyzed by carbon and oxygen isotopic values, rare earth element concentrations, and ⁸⁷Sr/⁸⁶Sr values to decode the genesis of the dissolved fractures and vugs.

3.1. Petrography and Cathodoluminescence

Key areas in 209 samples were marked and prepared for thin sections. Polarized and cross-polarized light were used to examine the pore space and associated diagenetic fabrics under a Zeiss Aixo Imager A2 microscope. Then, 60 samples displaying typical diagenetic fabrics were selected for a cathodoluminescence (CL) test to distinguish carbonate fabrics. Cathodoluminescence was performed on the CL8200 MK5-2 equipment, attached to the Zeiss microscope. The working condition of the electron gun is 14 V, 250 μA, and 0.003 mBar.

3.2. Fluid Inclusion Microthermometry

Based on the microscopic and cathodoluminescent observations, 27 samples were selected out and prepared for polished thin sections of 60 μm thickness. The fluid inclusion homogenization temperature (T_h) was measured to identify the diagenetic environments of calcite, quartz, and dolomite cements using a Linkam THMGS600 heating-freezing stage, at the Key laboratory of Tectonics and Petroleum Resources, China University of Geosciences, Wuhan. The cycling technique proposed by Goldstein and Reynolds [29] was used to measure Th in this study. The precision of the heating, cooling, and/or cycling intervals is 5 °C. Average value was calculated from at least five gas-fluid inclusions in one field of view as one datum of the representative Th of the tested cement.

3.3. Carbon and Oxygen Isotopes

The carbon and oxygen isotopic analyses of 52 powder samples micro-drilled from five types of rock fabrics were conducted on a Finnigan Mat 253 mass spectrometer at the Key Laboratory of Tectonics and Petroleum Resources in China University of Geosciences (Wuhan). The extraction of CO₂ from the 200-mesh powders of host rocks was performed

by anhydrous phosphoric acid (100%) in sealed tubes on an auto sample-handling machine at 72 °C for 2 h. All isotopic values which were calibrated with the Chinese national standards GBW04416 ($\delta^{13}\text{C} = +1.61 \pm 0.03\text{‰}$, $\delta^{18}\text{O} = -11.59 \pm 0.11\text{‰}$) and GBW04417 ($\delta^{13}\text{C} = -6.06 \pm 0.06\text{‰}$, $\delta^{18}\text{O} = -24.12 \pm 0.19\text{‰}$), and the international standards of NBS-18 ($\delta^{13}\text{C} = -5.01 \pm 0.06\text{‰}$, $\delta^{18}\text{O} = -23.0 \pm 0.1\text{‰}$) and NBS-19 ($\delta^{13}\text{C} = +1.95\text{‰}$, $\delta^{18}\text{O} = -2.20\text{‰}$). The acid fractionation factors used to calculate the isotope values were 1.01024 for calcite [30] and 1.00913 for dolomite [31]. All values were reported in per mil (‰) relative to Vienna Pee Dee Belemnite (VPDB). The precision and accuracy of the isotopic measurements are estimated to be better than 0.1‰.

3.4. Radiogenic Sr Isotopes

In total, 33 micro-drilling powder samples of five types of rock fabrics were selected out for radiogenic Sr isotopic ratio ($^{87}\text{Sr}/^{86}\text{Sr}$) measurements to analyze the nature and source of different episodes of diagenetic fluids. The measurements were conducted using a Nu plasma II MC-ICP-MS at the State Key Lab of Biogeology and Environmental Geology, Wuhan. Powders were digested by HCl and HNO₃ solution and the NIST SRM 987 standard with a mean value of 0.710223 ± 0.000034 (2SE) was employed. Standard error of our samples did not exceed 0.00001.

4. Results

4.1. Pore Types of Reservoir

The most prevalent pore type within the Lower Ordovician dolostones, as revealed by drilling core observations, is the half-filled fracture (Figure 3A). Microscopic examinations indicate that it primarily evolved from the dissolution along pre-existing calcite veins and fissures (Figure 3B–E). The secondary pore type observed within the cores is comprised of vugs (Figure 3F). Microscopic examinations exhibit embayed edges of dolomite crystals (Figure 3G) and smooth-edged calcite cements (Figure 3H). Apart from half-filled fractures and vugs, drill bit blowouts and drilling fluid losses during the drilling process hint at the existence of larger-scale pore spaces, possibly large fault zones or caverns that were inaccessible for coring, thus impeding observations at the core and thin-section scales.

4.2. Petrography of Reservoir Rocks

Petrographic observation reveals the deep buried Lower Ordovician dolostones are comprised mainly of six rock fabrics: dolomite matrix, pre-bitumen dolomite cements, calcite veins, dolomite breccias, quartz cements, and dolomite cements postdating solid bitumen (Figure 4).

The majority of the dolomite matrix is very dense, comprising microcrystalline and fine-crystalline dolomite (Figure 4A–C). This density arises from the interlocking contacts among dolomite crystals. In a few porous dolostones, euhedral fine-crystalline dolomite dominates, exhibiting cloudy cores with clear edges due to dolomite overgrowth. Solid bitumen emplacement occurs within the intercrystalline pores (Figure 4A). Another contributing factor to the matrix's density is the presence of coarse crystalline dolomite and quartz cements. Coarse crystalline dolomite had grown attached to pre-existing pores, while residual pore spaces were almost entirely filled by quartz cements (Figure 4B–D). Consequently, porosity within the dolomite matrix was minimal at the time of oil charging (Figure 4D).

Dissolution occurs not only in calcite veins and along fissures within the O₁P and O₁₋₂y¹ dolostones (Figure 3A–E), but also along stylolite and calcite veins in the overlying O₁₋₂y² limestones and dolomitic limestones (Figure 4E,F). Some other dolomite cements occupied into the dissolved fissures after the generation of solid bitumen (post-bitumen dolomite) (Figure 4G).

Fracturing is widespread, resulting mainly in the formation of calcite veins and fissures (Figure 3A–E) as well as brecciation (Figure 4H). Breccia dolostones exhibit typical terrestrially exposed features: carbonate vadose microspars, quartz sands (Figure 4I), and surface-derived allogenic kaolinite (Figure 4J). Besides these distinct diagenetic structures,

the most common fillings in breccia pores are calcite cements (Figure 4H). Notably, cathodoluminescent characteristics of these calcite cements vary; calcite cements in breccia pores in the southern TP193 well appears bright orange (Figure 4K,L), whereas in the northern S88 well, show no cathodoluminescence (Figure 4M,N).

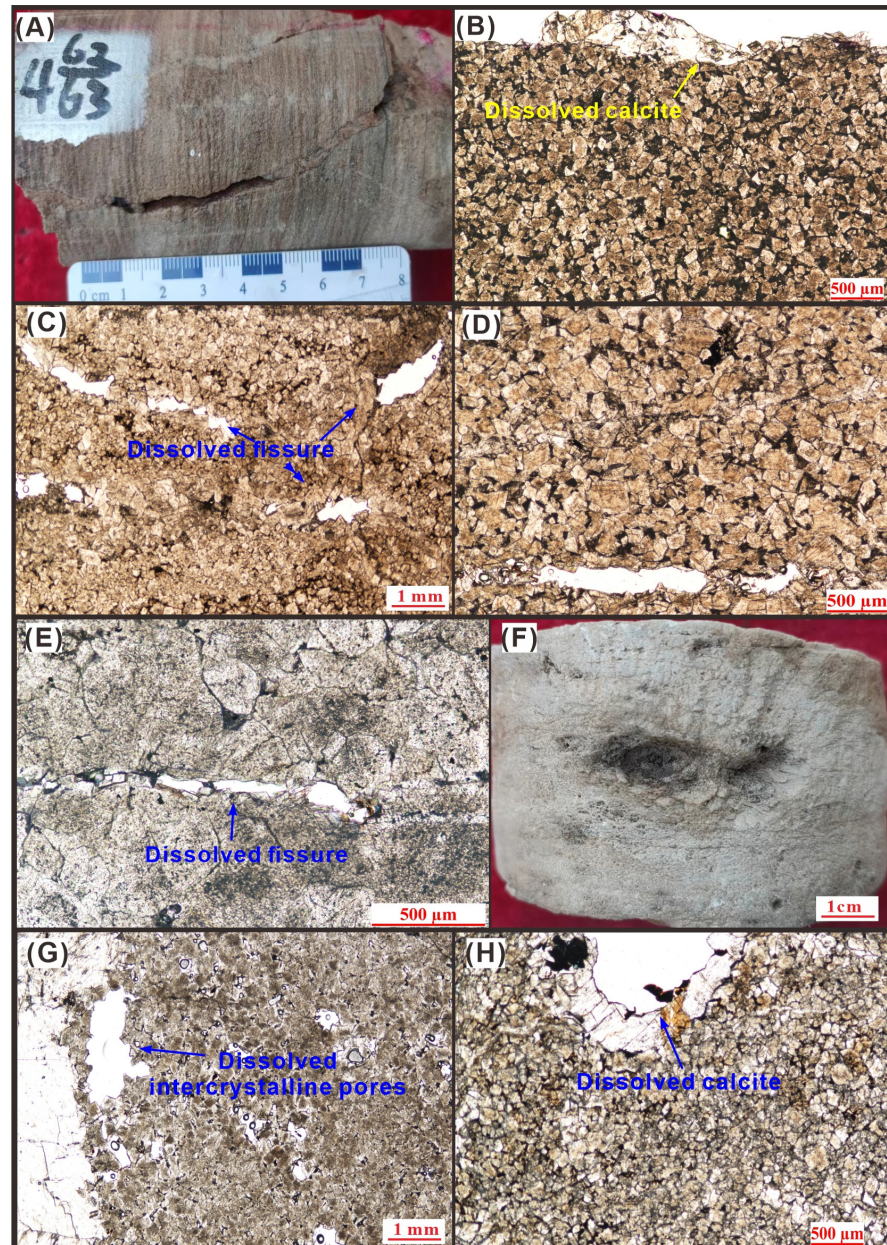


Figure 3. Petrographical characteristics of the reservoir dolostones at the drilling core and thin section scales. (A) High-angle fractures in dolostones, partially filled with calcite cements from TP193 well with depth of 7145.6 m. (B) Thin-section view displaying the pore space sourcing from the dissolution of calcite vein from TP193 well with depth of 7145.6 m. (C) Elongate vugs resulted from dissolution along fissures from S88 well with depth of 6457.8 m. (D) Fissure with the interrupted outline and smooth wall from TP193 well with depth of 7143.1 m. (E) Fissure with the interrupted outline and penetration into the dolomite crystals from SBP1 well with depth of 8451.5 m. (F) Vugs in dolostones from AD11 well with depth of 6705.1 m. (G) Thin-section view on the matrix of dolostones, noting that dolomite crystals around the intercrystalline pores were dissolved into embayed morphology from AD11 well with depth of 6705.1 m. (H) Calcite cements being dissolved and having smooth edge from AD11 well with depth of 6871.6 m.

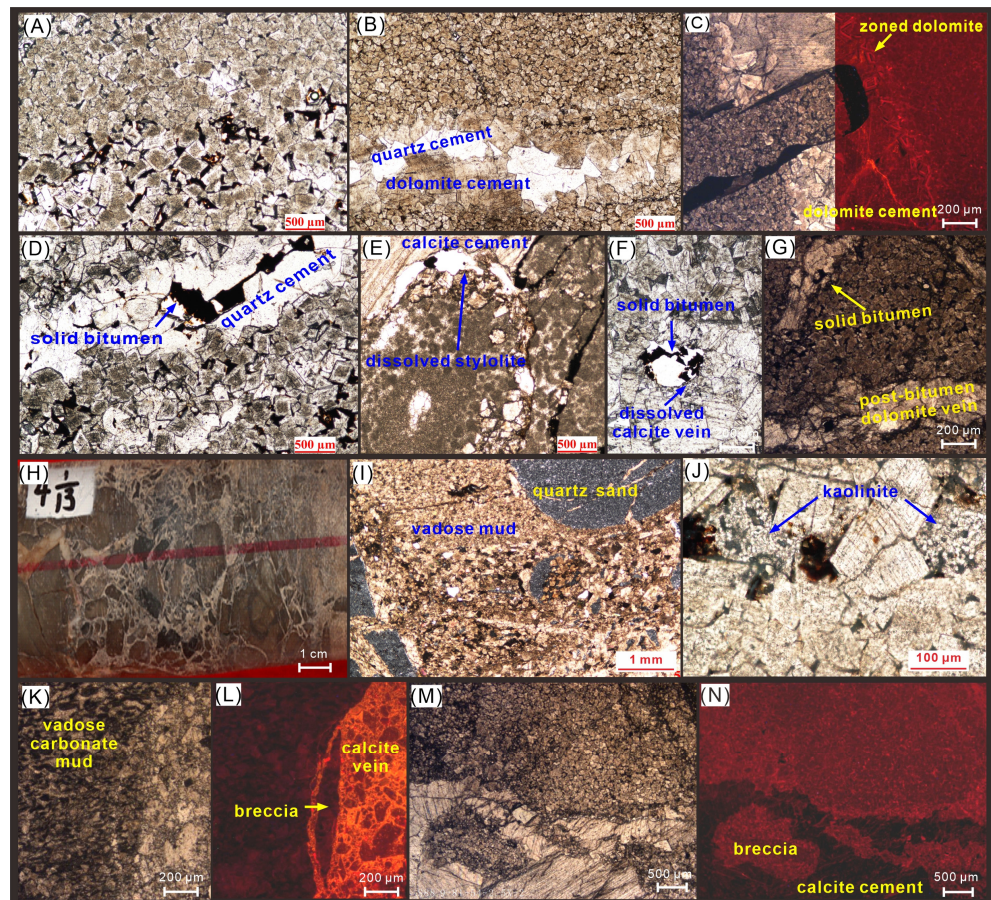


Figure 4. Petrography and cathodoluminescence of diagenetic products in the deep dolostones of the Lower Ordovician successions. (A) Fine-crystalline dolomite, dolomite overgrowth predating the solid bitumen from AD11 well with depth of 6709.8 m. (B) Fracture face lined with fine-crystalline overgrowing dolomite cements, then quartz cements filling the center of pore from TP193 well with depth of 7470.1 m. (C) Stylolite truncating the CL zoned overgrowing dolomite and dolomite veins from TP193 well with depth of 7383.2 m. (D) Solid bitumen emplacing the relict pores after SD and quartz cements from TP193 well with depth of 7382.7 m. (E) Dissolution along the stylolite in the Upper Yingshan limestone from TP193 well with depth of 7136.5 m. (F) Calcite crystals with embayed edge in a high-angle vein in the dolomitic limestones of the Upper Yingshan Formation, solid bitumen emplacing into the dissolution pore from AD11 well with depth of 6708.1 m. (G) Dolomite vein with a film of solid bitumen on the fracture face, solid bitumen also present in the intercrystalline pores from YQ2 well with depth of 6309.5 m. (H) Calcite cements (white color) in the inter-breccia pores from TS6 well with depth of 7080.2 m. (I) Terrigenous quartz sands and carbonate mud in the inter-breccia pores, cross-polarizes light from S88 well with depth of 6563.1 m. (J) Terrigenous kaolinite in the breccia dolomite from S88 well with depth of 6455.4 m. (K,L) polarized and cathodoluminescent light, calcite vein with dolomite breccia dropping out from the Wall rock, dolomite breccias and calcite cements showing dark red and bright orange luminescence respectively from TP193 well with depth of 7176.3 m. (M,N) Polarized and cathodoluminescent light, breccia dolomite with microspar matrix and calcite cements in the breccia pores, calcite cements showing non-luminescence from S88 well with depth of 6458.5 m.

4.3. Homogenization Temperature of Fluid Inclusions

The T_h in two types of calcite cements were measured. One type, calcite veins partially dissolved, yield 63 representative T_h data of biphasic inclusions, ranging from less than 60 °C to 160 °C, with the primary range between 60 °C and 120 °C (Figure 5A). The other type, found in breccia pores, has the major of single-phase fluid inclusions, and minor biphasic water-gas inclusions provide 8 representative T_h data, spanning from 70 °C to

120 °C, with peaks occurring at 70–80 °C and 100–110 °C (Figure 5B). The T_h ranges in both types of calcite cements are notably wide.

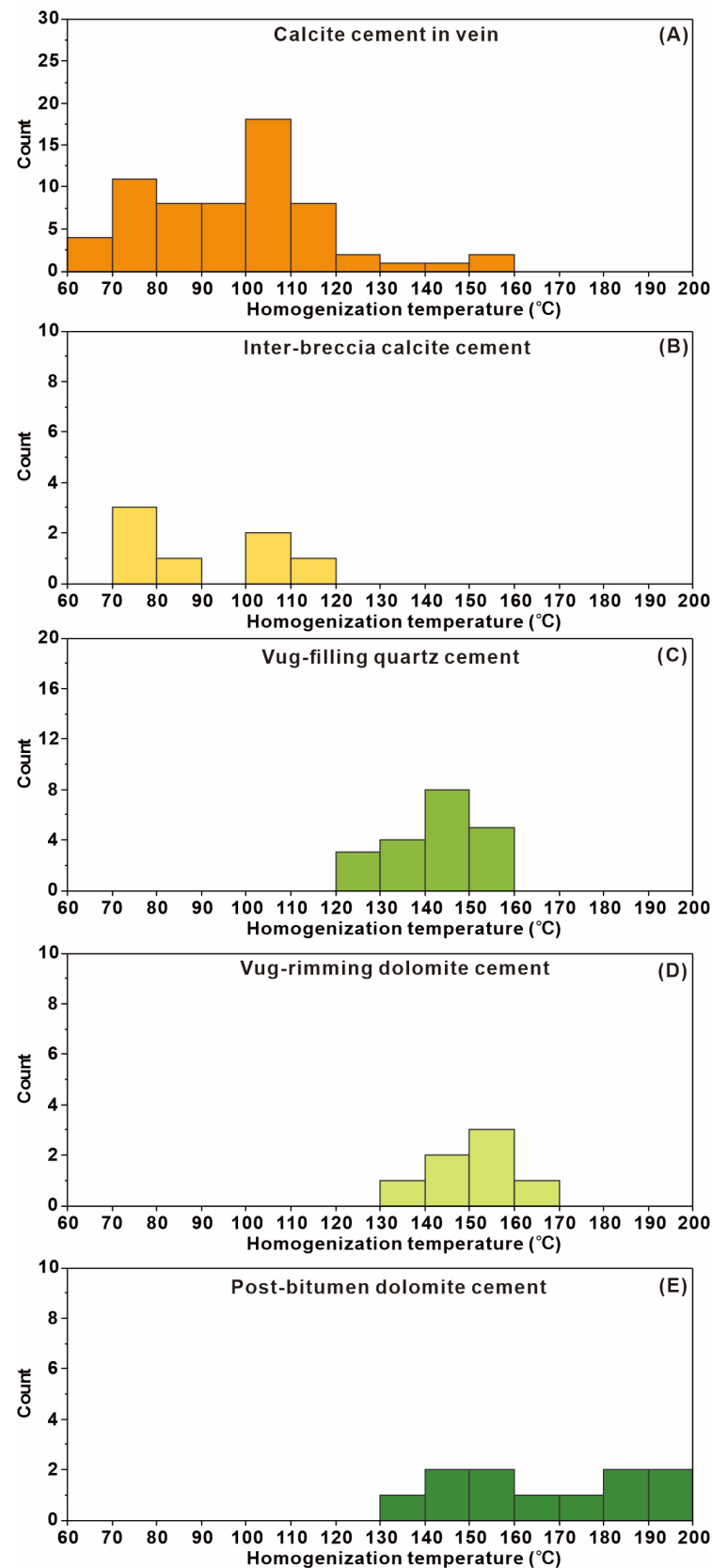


Figure 5. Homogenization temperature histograms of carbonate and quartz cements.

The T_h were also assessed for quartz cements. Twenty-one representative T_h were obtained, primarily grouping within the range of 120–160 °C (Figure 5C).

The T_h in two types of saddle dolomite were analyzed individually. One type, filling in pores and often coexisting with quartz cement, has T_h ranging from 130 °C to 170 °C, similar with the quartz cements (Figure 5D). The other type, post-bitumen dolomite cements, exhibited T_h ranging from 130 °C to 200 °C, displaying a broad range without peaks (Figure 5E).

4.4. Carbon and Oxygen Isotopic Ratios

The $\delta^{13}\text{C}$ and $\delta^{18}\text{O}$ values of five types of carbonate fabrics were identified (Figure 6). The microcrystalline dolomite matrix exhibits $\delta^{13}\text{C}$ values ranging from -1.6‰ to -2.3‰ and $\delta^{18}\text{O}$ values from -4.2‰ to -6.0‰ . Similarly, the fine-crystalline dolomite matrix displays $\delta^{13}\text{C}$ values from -1.6‰ to -2.4‰ and $\delta^{18}\text{O}$ values from -4.1‰ to -5.7‰ , closely to those of microcrystalline dolomite. Overgrowing fine-crystalline dolostones, characterized by conspicuous cloudy cores with clear edges, show $\delta^{13}\text{C}$ values from -1.5‰ to -2.6‰ and $\delta^{18}\text{O}$ values from -8.8‰ to -10.3‰ . Post-bitumen dolomite cements displayed $\delta^{13}\text{C}$ values ranging from -1.7‰ to -2.9‰ and $\delta^{18}\text{O}$ values from -6.7‰ to -9.7‰ .

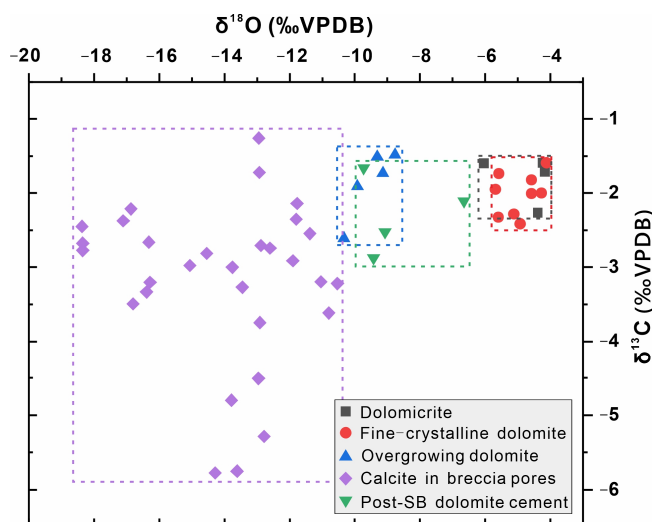


Figure 6. Carbon and oxygen isotopic values of typical carbonate fabrics.

Comparatively, the overgrowing fine-crystalline dolostones and post-bitumen dolomite exhibited $\delta^{13}\text{C}$ values close to or slightly more negative than those of the dolomite matrix, accompanied by significantly negative $\delta^{18}\text{O}$ values. Calcite cements within breccia pores portrayed the most negative $\delta^{13}\text{C}$ values (ranging from -1.3‰ to -5.8‰) and $\delta^{18}\text{O}$ values (ranging from -10.5‰ to -18.4‰) in contrast to the other fabrics.

4.5. Radiogenic Sr Isotopic Ratios

The $^{87}\text{Sr}/^{86}\text{Sr}$ values of five types of carbonate fabrics were examined (Figure 7). The microcrystalline dolomite matrix exhibit $^{87}\text{Sr}/^{86}\text{Sr}$ values ranged from 0.70888 to 0.70903, within the range of Early Ordovician seawater $^{87}\text{Sr}/^{86}\text{Sr}$ values (0.7085–0.7090). Overgrowing fine-crystalline dolostones display $^{87}\text{Sr}/^{86}\text{Sr}$ values ranged from 0.70905 to 0.70913, slightly higher than that of the Early Ordovician seawater. The fine-crystalline dolomite matrix exhibited $^{87}\text{Sr}/^{86}\text{Sr}$ values from 0.70905 to 0.70913, with some samples surpassing the Early Ordovician seawater values.

Calcite cements within breccia pores present a wider range of $^{87}\text{Sr}/^{86}\text{Sr}$ values, from 0.70871 to 0.71026. A few samples fall within the range of Early Ordovician seawater $^{87}\text{Sr}/^{86}\text{Sr}$ values, while most significantly surpass both Early Ordovician seawater and matrix dolostone $^{87}\text{Sr}/^{86}\text{Sr}$ values.

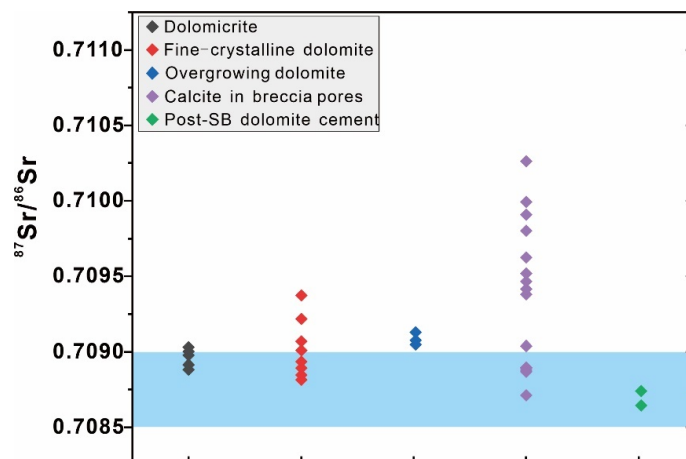


Figure 7. The $^{87}\text{Sr}/^{86}\text{Sr}$ values of typical carbonate fabrics in the lower Ordovician succession. The Ordovician seawater $^{87}\text{Sr}/^{86}\text{Sr}$ values (0.7084–0.7090) in the blue zone from reference [32].

Post-bitumen dolomite cements, represented by two samples, have $^{87}\text{Sr}/^{86}\text{Sr}$ values of 0.70864 and 0.70874, falling within the range of Early Ordovician seawater $^{87}\text{Sr}/^{86}\text{Sr}$ values but lower than the matrix dolostone $^{87}\text{Sr}/^{86}\text{Sr}$ values.

5. Discussion

5.1. Paragenetic Sequence in Reservoir Rocks

Veins and breccia-pore fillings markedly differ in mineralogy and crystal size from the surrounding dolostones, suggesting an early occurrence of dolomitization. The overgrowth of dolomite crystals with cloudy cores and clear edges along the wall of pores and fractures often indicates the slow process during burial following dolomitization as temperatures gradually increased (Figure 4A–D).

Stylolite, a common product of chemical compaction, is the perfect indicator of paragenetic sequences [33]. Calcite veins crosscutting limestone and dolomitic limestone formed before or during chemical compaction (Figure 4E,F) [34,35]. The ranges of fluid inclusions in dissolved calcite veins indicate their precipitation in shallow-medium burial environments (Figure 5A). Furthermore, the wide ranges of T_h suggest the prolonged precipitation, likely as products of chemical compaction by which carbonate grains and crystals dissolved at their contact, then reprecipitated in other pore space from syn-sedimentation to the Late Ordovician (Figure 5A).

The context of pore-filling materials from wall to center of pore space aids in delineating the diagenetic paragenetic sequence. Coarse-crystalline dolomite cements on pore walls and quartz cements in the center exhibit some kind of temporal order (Figure 4B). However, their common coexistence in this study area and similar high T_h values indicate successive precipitates at one episode of fluid activity (Figure 5C,D). The solid bitumen emplacement into the center of residual pores suggests that coarse-crystalline dolomite and quartz precipitated before oil charging (Figure 4D).

Considering the burial history, thermal history, and oil charging history of the south of the Tabei Uplift, three phases of oil charging occurred around 233–210 Ma, 138–123 Ma, and 21–13 Ma, respectively (Figure 8). Prior to oil charging in the Tarim Basin, hot fluid activities depositing quartz are widely considered to have occurred in the Late Permian volcanic activity (Figure 8) [36–38]. The wide range of T_h in post-bitumen dolomite also suggests its precipitation during a prolonged, rather than episodic, diagenetic process (Figure 5E). Furthermore, with $\delta^{13}\text{C}$ and $^{87}\text{Sr}/^{86}\text{Sr}$ values close to those of the wall rock and more negative $\delta^{18}\text{O}$, we speculate that post-bitumen dolomite cements sourced from chemical compaction during the Early Cretaceous or the Neogene-Quaternary period, driven by the increasing overburden pressure as rapid sedimentation (Figure 8).

The appearance of bitumen in dissolved intracrystalline pores within calcite crystals indicates that dissolution occurred after chemical compaction of limestone and before bitumen generation (Figure 4F). During this period, the most probable corrosive fluids were meteoric freshwater from the Middle Ordovician to the Devonian (Figure 8) [39]. Evidence of freshwater activities, besides dissolved calcite veins and incomplete dolomite crystals, includes microspar in breccia pores, quartz sand, allogenic kaolinite, and significantly negative $\delta^{18}\text{O}$ and anomaly high $^{87}\text{Sr}/^{86}\text{Sr}$ values of calcite cements within breccia pores (further detailed discussion below).

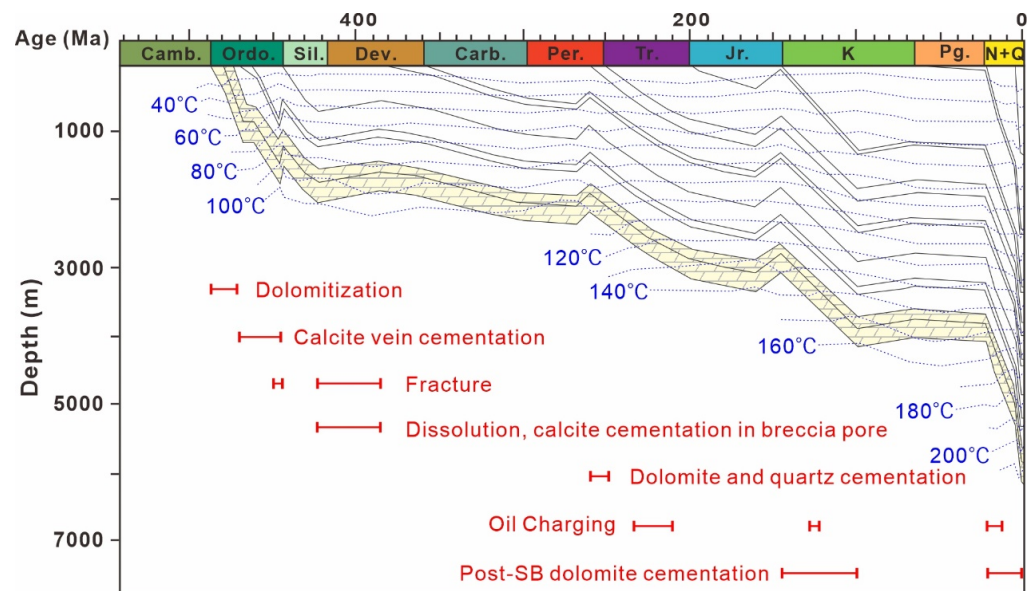


Figure 8. Paragenetic sequence in the deep Lower Ordovician succession. The framework of burial and thermal history of the southern Tabei Uplift for reference [40].

5.2. Pore Space Development and Karst Dissolution

Although the Lower Ordovician dolostones in the southern area have never been exposed at the surface, there are lines of evidence that corrosive fluids originated from the meteoric freshwater rather than from formation fluids or hydrothermal fluids. Mineralogical indications of meteoric infiltration were identified, such as quartz sand and allogenic kaolinite, which are distinct from hydrothermal minerals.

Furthermore, the geochemistry of karst calcite cements, including $\delta^{13}\text{C}$, $\delta^{18}\text{O}$, $^{87}\text{Sr}/^{86}\text{Sr}$, and rare earth elements, have been proven to be useful tools for analyzing karst fluid properties, investigating karst processes, or ancient hydrology of karst systems [41–43]. Oxygen isotopic fractionation in carbonates is controlled by both temperature and the $\delta^{18}\text{O}$ of precipitating fluids. Highly negative $\delta^{18}\text{O}$ values are generally interpreted as originating from freshwater or extremely high-temperature hydrothermal fluids [39,44].

While the Th (70–120 °C) of calcite in breccia pores indicate precipitation environments distinctly below the surface, the calculated $\delta^{18}\text{O}_{\text{SMOW}}$ values of fluids based on Th and $\delta^{18}\text{O}_{\text{PDB}}$ of calcite fall within the range of freshwater and Ordovician seawater, indicating a freshwater source buffered by wall rocks and formation water (Figure 9). Hence, the higher Th of breccia-pore calcite in the southern study area may result from deeper infiltration of freshwater gradually heated. Zhang et al. and Han et al. reported the most negative values of cave-filling calcite beneath the unconformity surface in the Tarim Oilfield, reaching -15.3‰ and -15.0‰ , respectively [39,44]. This study discovered even more negative values (-18.4‰) in the TP193 well further south. Moreover, the increasing trend of Th and $\delta^{18}\text{O}_{\text{PDB}}$ towards the south validates the gradual heating during the process of freshwater infiltration (Figure 10).

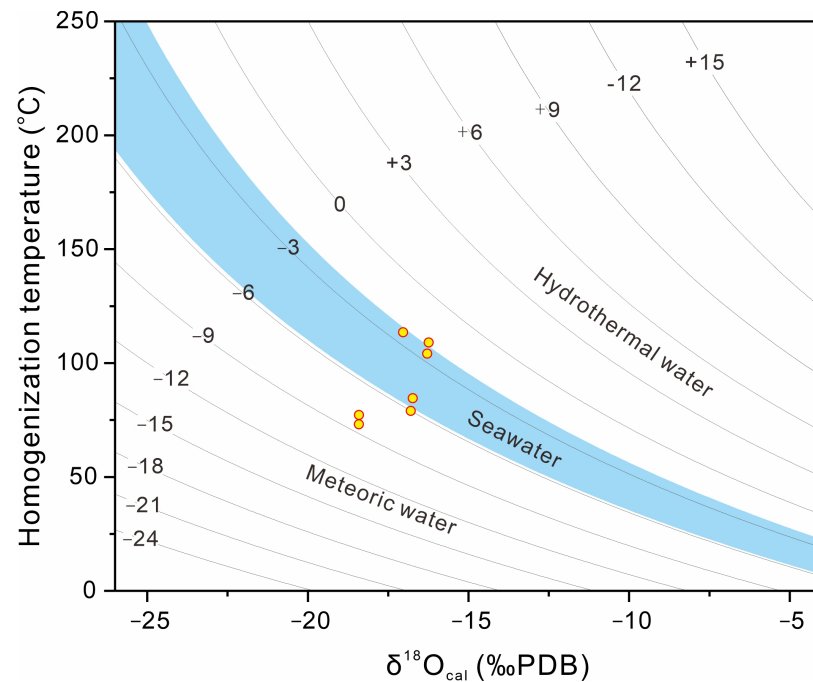


Figure 9. $\delta^{18}\text{O}_{\text{SMOW}}$ values of diagenetic water calculated from the homogenization temperature (black dash lines) and $\delta^{18}\text{O}_{\text{PDB}}$ values of calcite cements in inter-breccia pores and high-angle veins (solid circles), using the calcite-water oxygen isotope fractionation equation: $10^3 \times \ln\alpha_{\text{cal-water}} = 2.789 \times 10^6 \times T^{-2} - 2.89$ [30]. $\delta^{18}\text{O}_{\text{SMOW}}$ values of the Ordovician seawater ranges from -5.8‰ to -2.2‰ from Veizer et al. [32].

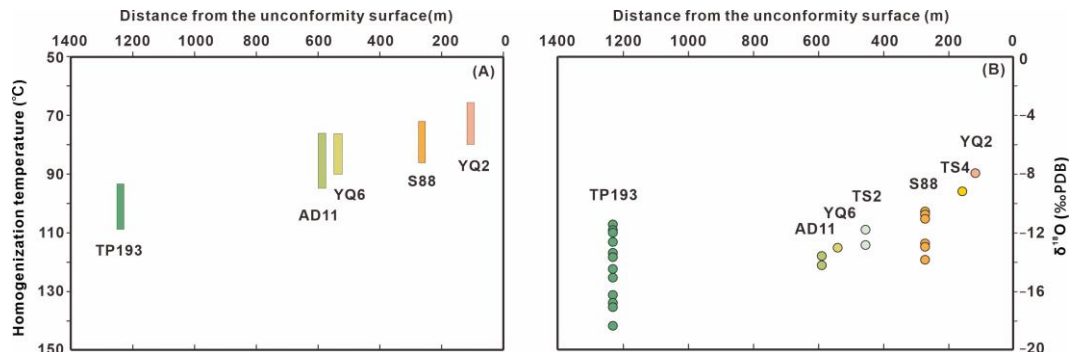


Figure 10. Homogenization temperature (A) and $\delta^{18}\text{O}$ data (B) of calcite cements in inter-breccia pores and high-angle veins of wells from north to south variation with the distance from the unconformity surface.

The $^{87}\text{Sr}/^{86}\text{Sr}$ values of meteoric freshwater is related to the lithology of exposed successions. In the Tabai Uplift, the anomalously high $^{87}\text{Sr}/^{86}\text{Sr}$ values of cave-filling calcite are considered to be representative evidence of Devonian meteoric freshwater percolating through the exposed Silurian sandstones, whereas the Middle and Late Ordovician marine carbonate rocks exposed at the end of the Middle Ordovician cannot yield $^{87}\text{Sr}/^{86}\text{Sr}$ values above 0.7100 in karst calcite cements. Indeed, Zhang et al. measured the $^{87}\text{Sr}/^{86}\text{Sr}$ ratios of Late Middle Ordovician-formed calcite, which were lower than 0.7094 [45], confirming this point. Probably due to the mixing of this freshwater with formation water, recrystallized or overgrowing dolomite also shows slightly higher $^{87}\text{Sr}/^{86}\text{Sr}$ than the dolomite matrix.

5.3. Distribution of Reservoir and Freshwater Channel

The distribution relationship between dissolved veins, fissures, and vugs at the micro scale resonates with the intimate relationship between faults and reservoir distribution,

indicated by string-like anomalous bodies on seismic profiles (Figure 11). Typical seismic reflection characteristics of karst reservoirs in the northern Tarim Basin manifest as “bright spots”, characterized by strong reflection amplitudes, long longitudinal extensions, and small horizontal ranges, resulting from strong impedance differences between the reservoir and the surrounding dense rocks [46,47]. Previous studies, based on seismic “bright spots” calibrated with drilling cores and imaging logging, identified carbonate karst fault reservoirs in the southern part of the Tarim Uplift [28].

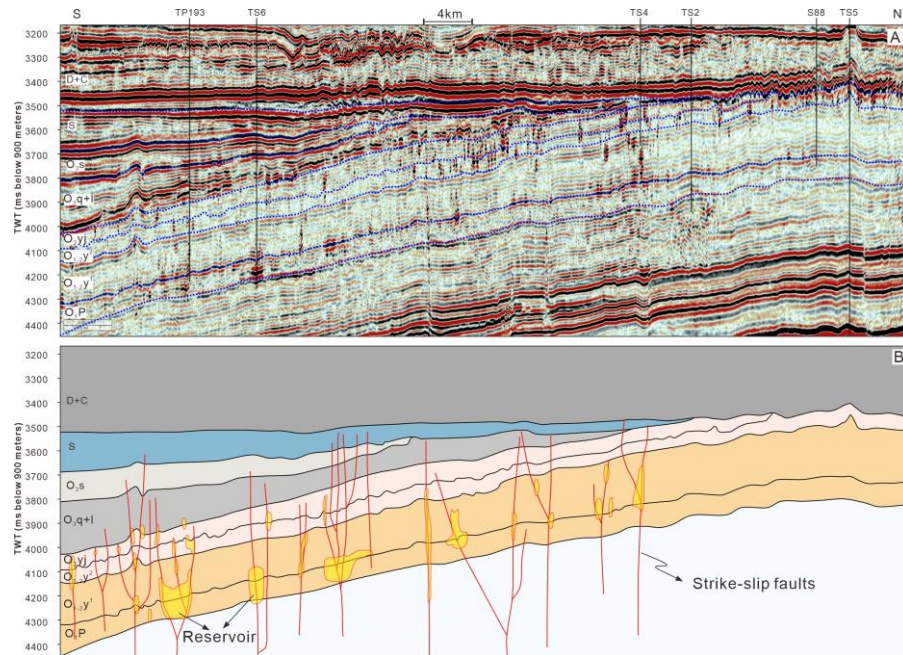


Figure 11. Distribution of reservoirs recognized as bright spots of the seismic abnormal bodies and strike-slip faults. (A) The seismic profile. (B) The geologic interpretation of strike-slip faults and reservoirs.

Observing the north-south seismic profiles in the northern part of the Tarim Uplift (north of TS4), bright spot reflections are distributed in a planar pattern in the Middle-Lower Ordovician exposed areas and near the Upper Ordovician strata pinch-out line, confined primarily in the middle Ordovician ($O_{1-2}y^1$ and O_2y) and without extending to the Lower Ordovician (O_{1p} and $O_{1-2}y^1$). This distribution pattern has been interpreted as a product of near-surface karstification [39,48]. Conversely, in the southern region (south of TS4), bright spot reflections are scattered throughout the Middle-Lower Ordovician strata. The distribution of karst reservoirs in the southern region evidently cannot be explained by near-surface karstification models, as the overlying upper Ordovician consists of non-karstic layers (O_{3q} – O_{3s}), and the Middle-Lower Ordovician cannot be directly percolated by downward-flowing freshwater [48]. Excluding the near-surface karstification, two possible hydrogeological schemes of karstification can explain the reservoir distribution in non-exposed areas: (i) freshwater percolating down along the fracture system into $O_{1-2}y^2$ limestone and (ii) lateral movement of atmospheric precipitation along permeable strata from the exposed area in the north [39].

The first scenario demonstrates higher potential. Superimposing the distribution of faults in the study area, the reservoirs exhibit distributions along faults, most of which are strike-slip faults (Figure 11) [28,49]. This indicates that the karst channels of meteoric freshwater resulting in reservoir development shifts from surface runoffs and underground rivers in the northern region to these strike-slip faults. As oxidative surface freshwater infiltrates deeper, its reducing nature gradually intensifies, resulting in brighter cathodoluminescence of breccia pore-filling calcite in the southern part and no cathodoluminescence in the northern region (Figure 4K–N). The Late Ordovician to early Silurian was the primary period for the development of basement strike-slip faults in the Tarim Basin [50–52]. The

termination of these strike-slip faults upwards into the Silurian strata in the study area also indicates that karstification may have occurred from the Silurian to the Devonian periods (Figure 11).

5.4. Genesis of Vuggy and Fractured Dolostone Reservoir

The differences in reservoir distribution between the southern and northern regions of the Tabei Uplift reveal two distinct models of karst reservoir development under different hydrological frameworks. In the Late Ordovician (O_{3s}) period, karstification primarily occurred in the northern part of the Tarim Uplift where the Middle Ordovician was exposed, the development and distribution of reservoirs were controlled by rock fissures and ancient water tables. At the periphery of the exposed area, artesian meteoric freshwater laterally flowed through the Middle Ordovician, forming an underground river system, complementing the type of karst reservoirs (Figure 12A).

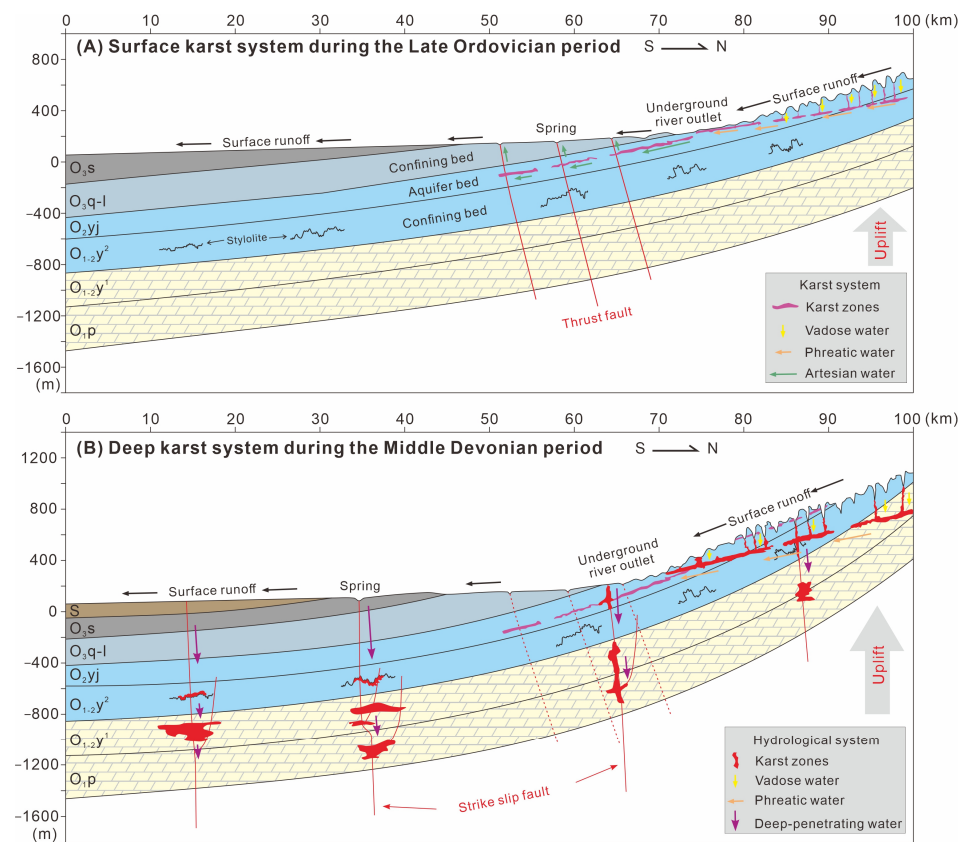


Figure 12. Schematic models show the hydrology and reservoir distributions during two episodes of meteoric karstification. **(A)** Reservoirs developed beneath the unconformity surface and peripheral artesian area in the surface karst system during the late Caledonian period. **(B)** Reservoirs developed along the strike-slip faults in the whole Tabei Uplift.

During the Devonian (D_1), the northern region underwent further uplift. Overlying the pre-existing karst system, a new phase of karst modification was added. In contrast, in the southern region, meteoric freshwater seeped into the Middle-Lower Ordovician strata along fractures directly connected to the surface due to gravity. This infiltration occurred along fractures, fissures, pre-existing pores as well as stylolites, resulting in the dissolution of carbonate wall rocks, forming karstic fault reservoirs distributed along faults (Figure 12B).

6. Conclusions

This paper identified the pore space type and supposed that dissolution was responsible for the development of the pore space in the southern region of the northern Tarim Basin. A karst model was established to interpret the genesis of the deep burial dolostone reservoir based on the distribution of reservoirs and nature of dissolving fluid.

- (1) The Lower Ordovician dolostone reservoirs in the southern part of the Tabei uplift exhibit pore space characterized by fractures and vugs. Based on the petrographical, cathodoluminescent, and fluid inclusion microthermometric characteristics of carbonate and quartz fabrics, we built up the diagenetic paragenetic sequence. It indicates that prior to the occurrence of dissolution creating the pore space, the strata had already reached a certain depth (as evidenced by the stylolites in the overlying limestones).
- (2) Inter-breccia calcite cements act as the key clue for the nature of dissolving fluid in this study. Isotopic analyses reveal that the fluid responsible for the dissolution was sourced from meteoric freshwater during the Devonian period.
- (3) At the micro scale, dissolution often manifests as the dissolution and enlargement of pre-existing calcite cements and fractures. At the macroscale, seismic reflections of karstic fault reservoirs distinctly demonstrate distribution along strike-slip faults. This reservoir distribution features at different scales which collectively indicate that faults serve as karst channels for meteoric freshwater dissolution in the southern part of the Tarim Uplift.
- (4) The formation of karstic fault reservoirs in the southern Tarim Basin uplift is influenced by the formation of strike-slip faults and exposure of the overlying strata to the surface. Meteoric freshwater from the surface percolated downward along deep-seated strike-slip faults, causing dissolution in the unexposed Middle-Lower Ordovician strata. This process resulted in the formation of string-like karstic fault reservoirs distributed along strike-slip faults.

These understandings evoke the role of the strike-slip faults, which acted as conduits of deep karstification and controlled the distribution of reservoirs. This is important for energy exploration and production at this study area in the future.

Author Contributions: Author Contributions: Conceptualization, L.G. and G.L.; methodology, J.L.; software, J.L.; validation, L.G., J.L. and Y.L.; formal analysis, G.L. and J.L.; investigation, G.L. and J.L.; resources, L.G., Y.L. and G.L.; data curation, J.L.; writing—original draft preparation, J.L. and G.L.; writing—review and editing, J.L. and L.F.; visualization, G.L. and J.L.; supervision, J.L., L.F. and G.L.; project administration, L.G., Y.L. and G.L.; funding acquisition, L.G., Y.L. and G.L. All authors have read and agreed to the published version of the manuscript.

Funding: This research was funded by National Natural Science Foundation of China, grant number 42002170, SINOPEC Research Project P21048-2 and National Key R&D Program of China, grant number 2017YFC0603104 and 2019YFC0605502.

Data Availability Statement: All data have been reported in the text.

Conflicts of Interest: Authors Lijun Gao and Yongli Liu are employed by the Sinopec Northwest Oil Field Company. Author Jie Li was charged with the responsibility to the National Natural Science Foundation of China and National Key R&D Program of China. Authors Guorong Li and Liyun Fu were scientific advisers responsible for the SINOPEC Research Project. The remaining authors declare that the research was conducted in the absence of any commercial or financial relationships that could be construed as a potential conflict of interest.

References

1. Ford, D.C.; Ewers, R.O. The development of limestone cave systems in the dimensions of length. *Can. J. Earth Sci.* **1978**, *15*, 1783–1798. [[CrossRef](#)]
2. He, Y.B. Hydrodynamic Profile of Homogeneous Thick Limestone and Its Practical Significance. *China Karst* **1991**, *4*, 1–12.
3. Ford, D.C.; Williams, P.W. *Karst Hydrogeology and Geomorphology*; Wiley: Chichester, UK, 2007; 562p.

4. Zhang, B.M.; Liu, J.J. Classification and characteristics of karst reservoirs in China and related theories. *Pet. Explor. Dev.* **2009**, *36*, 12–31.
5. Fritz, R.D.; Medlock, P.; Kuykendall, M.J.; Wilson, J.L. The Geology of the Arbuckle Group in the Midcontinent: Sequence Stratigraphy, Reservoir Development, and the Potential for Hydrocarbon Exploration. In *AAPG Annual Convention and Exhibition, Pittsburgh, Pennsylvania, Search and Discovery Article*; The American Association of Petroleum Geologists: Tulsa, OK, USA, 2013; p. 30266.
6. King, B.D.; Goldstein, R.H. History of hydrothermal fluid flow in the midcontinent, USA: The relationship between inverted thermal structure, unconformities and porosity distribution. In *Reservoir Quality of Clastic and Carbonate Rocks: Analysis, Modelling and Prediction*; Armitage, P.J., Butcher, A.R., Churchill, J.M., Csoma, A.E., Hollis, C., Lander, R.H., Omma, J.E., Worden, R.H., Eds.; Geological Society, Special Publications: London, UK, 2018; Volume 435, pp. 283–320.
7. Medici, G.; Lorenzi, V.; Sbarbati, C.; Manetta, M.; Petitta, M. Structural classification, discharge statistics, and recession analysis from the springs of the Gran Sasso (Italy) carbonate aquifer; comparison with selected analogues worldwide. *Sustainability* **2023**, *15*, 10125. [[CrossRef](#)]
8. Brett, C.E.; Goodman, W.M.; Loduca, S.T.; Tetreault, D. Silurian–Early Devonian sequence stratigraphy, events, and paleoenvironments of western New York and Ontario, Canada. In *New York State Geological Association 71st Annual Meeting, Field Trip Guidebook*; Department of Geosciences SUNY College: Fredonia, NY, USA, 1999.
9. Loucks, R.G. *Review of the Lower Ordovician Ellenburger Group of the Permian Basin, West Texas*; Ellenburger Draft; Online; 2008; 95p.
10. Davies, G.; Smith, L. Structurally controlled hydrothermal dolomite reservoir facies: An overview. *AAPG Bull.* **2006**, *90*, 1641–1690. [[CrossRef](#)]
11. Ford, D.C. Karst geomorphology, caves and cave deposits: A review of North American contributions during the past half century. In *Perspectives on Karst Geomorphology, Hydrology and Geochemistry*; GSA Special Paper, 404; Harmon, R.S., Wicks, C.W., Eds.; John Wiley & Sons: Boulder, Colorado, USA, 2006; pp. 1–14.
12. Klimchouk, A. Morphogenesis of hypogenic caves. *Geomorphology* **2009**, *106*, 100–117. [[CrossRef](#)]
13. Kang, Z.J. Cases of Discovery and Exploration of Marine Fields in China (Part 4): Tahe Oilfield in Tarim Basin. *Mar. Oil Gas Geol.* **2005**, *10*, 31–38.
14. Zhou, X.Y.; Yang, H.J.; Han, J.F.; Wang, F.H.; Han, J. Cases of Discovery and Exploration of Marine Fields in China (Part 12): Lunnan Ordovician Oil-Gas Field in Tarim Basin. *Mar. Oil Gas Geol.* **2009**, *14*, 67–77.
15. Zhu, G.Y.; Zhang, S.C.; Zhang, B. Reservoir types of marine carbonates and their accumulation model in western and central China. *Acta Pet. Sin.* **2010**, *31*, 871–878.
16. Derby, J.; Fritz, R.; Longacre, S.; Morgan, W.; Sternbach, C. *The Great American Carbonate Bank: The Geology and Economic Resources of the Cambrian–Ordovician Sauk Megasequence of Laurentia*; AAPG Memoir; AAPG: Tulsa, OK, USA, 2012; Volume 98, 1210p.
17. Yan, W.; Wang, X.Z.; Ding, Y. The discovery and characteristics of covered-pressurization karst during early Hercynian in south Tahe oilfield. *J. Southwest Pet. Univ. (Sci. Technol. Ed.)* **2011**, *33*, 53–60.
18. Lyu, Y.P.; Zhao, X. Study on reservoir forming mechanism and development mode of distribution of Ordovician carbonate in the southeast slope area of Tahe oilfield. *J. Mineral. Petrol.* **2012**, *32*, 107–115.
19. Han, C.C.; Lin, C.Y.; Ren, L.H.; Lu, X.B.; Wei, T.; Zhang, X. Characteristics of Ordovician fault in the Block 10 of Tahe Oilfield, Tarim Basin and its controlling effect on karst reservoirs. *Nat. Gas Geosci.* **2016**, *27*, 790–798.
20. Li, H.; Li, G.R.; Luo, Y.; Fu, H.; Gao, Y.W.; Zhu, Y.Y.; Zhang, W. Characteristics of Hydrothermal Fluid in Deep Ordovician Carbonate Reservoirs in Tahe Area. *J. Northeast Pet. Univ.* **2014**, *38*, 12–23.
21. Jia, C.Z. *Structural Characteristics and Oil and Gas in Tarim Basin*; Petroleum Industry Press: Beijing, China, 1997; 438p.
22. Zhang, G.Y.; Zhao, W.Z.; Wang, H.J.; Li, H.H.; Liu, L. Multicycle tectonic evolution and composite petroleum systems in the Tarim Basin. *Oil Gas Geol.* **2007**, *28*, 653–663.
23. Meng, X.X.; Wang, H.B.; Yao, Q.Z. Tectonic Evolution Characteristics of Tabei Uplift and Its Controlling Effect on the Reservoir and Hydrocarbon Accumulation of Ordovician Carbonate. *Nat. Gas Geosci.* **2015**, *26*, 109–120.
24. He, D.F.; Jia, C.Z.; Li, D.S.; Zhang, C.J.; Meng, Q.R.; Shi, X. Formation and evolution of polycyclic superimposed Tarim Basin. *Oil Gas Geol.* **2005**, *26*, 64–77.
25. Qi, L.X.; Yun, L. Development characteristics and main controlling factors of the Ordovician carbonate karst in Tahe oilfield. *Oil Gas Geol.* **2010**, *31*, 1–12.
26. Lyu, H.T.; Zhang, D.J.; Yang, Y.C. Stages of Paleokarstic Hypergenesis in Ordovician Reservoir, Tahe Oilfield. *Geol. Sci. Technol. Inf.* **2009**, *28*, 71–75, 83.
27. Lin, C.S.; Li, S.T.; Liu, J.Y.; Qian, Y.; Luo, H.; Chen, J.; Peng, L.; Rui, Z. Tectonic framework and paleogeographic evolution of the Tarim basin during the Paleozoic major evolutionary stages. *Acta Petrol. Sin.* **2011**, *1*, 210–218.
28. Lu, X.; Wang, Y.; Tian, F.; Li, X.; Yang, D.; Li, T.; Lv, Y.; He, X. New Insights into the Carbonate Karstic Fault System and Reservoir Formation in the Southern Tahe Area of the Tarim Basin. *Mar. Pet. Geol.* **2017**, *86*, 587–605. [[CrossRef](#)]
29. Goldstein, R.H.; Reynolds, T. *Systematics of Fluid Inclusions in Diagenetic Minerals*; Society for Sedimentary Geology: Tulsa, OK, USA, 1994.
30. Friedman, I.; O’Neil, J.R. *Data of Geochemistry: Compilation of Stable Isotope Fractionation Factors of Geochemical Interest*; US Government Printing Office: Washington, DC, USA, 1977.

31. Rosenbaum, J.; Sheppard, S. An isotopic study of siderites, dolomites and ankerites at high temperatures. *Geochim. Cosmochim. Acta* **1986**, *50*, 1147–1150. [[CrossRef](#)]
32. Veizer, J.; Ala, D.; Azmy, K.; Bruckschen, P.; Buhl, D.; Bruhn, F.; Carden, G.A.; Diener, A.; Ebner, S.; Godderis, Y.; et al. $^{87}\text{Sr}/^{86}\text{Sr}$, $\delta^{13}\text{C}$ and $\delta^{18}\text{O}$ evolution of Phanerozoic seawater. *Chem. Geol.* **1999**, *161*, 59–88. [[CrossRef](#)]
33. Lu, Z.; Chen, H.; Qing, H.; Chi, G.; Chen, Q.; You, D.; Yin, H.; Zhang, S. Petrography, Fluid Inclusion and Isotope Studies in Ordovician Carbonate Reservoirs in the Shunnan Area, Tarim basin, NW China: Implications for the Nature and Timing of Silicification. *Sediment. Geol.* **2017**, *359*, 29–43. [[CrossRef](#)]
34. Li, J.; Cai, Z.X. The Role of Seal and Source Rocks in Fluid-rock Interactions and their Reservoir Effects within the Carbonate Deep Burial Realm. *Acta Geol. Sin. (Engl. Ed.)* **2022**, *96*, 1353–1361. [[CrossRef](#)]
35. Li, J.; Cai, Z.X. *Development and Preservation Mechanism of Deep High-Quality Dolostone Reservoirs*; University of Geosciences Press: Wuhan, China, 2022; 147p.
36. Dong, S.F.; Chen, D.Z.; Qing, H.R.; Zhou, X.; Wang, D.; Guo, Z.; Jiang, M.; Qian, Y. Hydrothermal alteration of dolostones in the Lower Ordovician, Tarim Basin, NW China: Multiple constraints from petrology, isotope geochemistry and fluid inclusion microthermometry. *Mar. Pet. Geol.* **2013**, *46*, 270–286. [[CrossRef](#)]
37. Jin, Z.J.; Zhu, D.Y.; Meng, Q.Q.; Hu, W. Hydrothermal activities and influences on migration of oil and gas in Tarim Basin. *Acta Petrol. Sin.* **2013**, *29*, 1048–1058.
38. Zhu, D.Y.; Meng, Q.Q.; Jin, Z.J.; Liu, Q.; Hu, W. Formation mechanism of deep Cambrian dolomite reservoirs in the Tarim basin, northwestern China. *Mar. Pet. Geol.* **2015**, *59*, 232–244. [[CrossRef](#)]
39. Zhang, Y.M.; Zhang, S.N.; Huang, B.W.; Lu, Z.; Ye, N.; Zhu, B.; Hou, X.; Xie, F.; Bai, X.; Zhang, X. Fluid Inclusion, Isotopic, and Elemental Geochemistry Studies of Cave-Filling Calcite in the Lower–Middle Ordovician Yingshan Formation of Tahe Oilfield, NW China: Implication for Karstification in Non-exposed Limestone. *Front. Earth Sci.* **2022**, *10*, 842386. [[CrossRef](#)]
40. Feng, T. Analysis on the Difference of Hydrocarbon Accumulation of the Ordovician in Tahe Area and Its Peripheral Area, Tarim Basin. Master's Thesis, Yangtze University, Jingzhou, China, 2023; 67p.
41. Rossi, C.; Goldstein, R.H.; Ceriani, A.; Marfil, R. Fluid Inclusions Record thermal and Fluid Evolution in Reservoir Sandstones, Khataba Formation, Western Desert, Egypt: A Case for Fluid Injection. *AAPG Bull.* **2002**, *86*, 1773–1799.
42. Ainsaar, L.; Kaljo, D.; Martma, T. Middle and Upper Ordovician Carbon Isotope Chemostratigraphy in Baltoscandia: A Correlation Standard and Clues to Environmental History. *Palaeogeogr. Palaeoclimatol. Palaeoecol.* **2010**, *294*, 189–201. [[CrossRef](#)]
43. Bourdin, C.; Douville, E.; Genty, D. Alkaline-Earth Metal and Rare Earth Element Incorporation Control by Ionic Radius and Growth Rate on a Stalagmite from the Chauvet Cave, Southeastern France. *Chem. Geol.* **2011**, *290*, 1–11. [[CrossRef](#)]
44. Han, C.; Lin, C.; Lu, X.; Tian, J.; Ren, L.; Ma, C. Petrological and Geochemical Constraints on Fluid Types and Formation Mechanisms of the Ordovician Carbonate Reservoirs in Tahe Oilfield, Tarim Basin, NW China. *J. Pet. Sci. Eng.* **2019**, *178*, 106–120. [[CrossRef](#)]
45. Zhang, T.; Yun, L.; Wu, X.; Ye, D. The Application of Strontium Isotopes in Division of Paleokarst Stages in Tahe Oilfield. *Pet. Geol. Explor.* **2005**, *27*, 299–303.
46. Zeng, H.L.; Wang, G.; Janson, X.; Loucks, R.; Xia, Y.; Xu, L.; Yuan, B. Characterizing seismic bright spots in deeply buried, Ordovician paleokarst strata, central Tabei Uplift, Tarim basin, western China. *Geophysics* **2011**, *76*, B127–B137. [[CrossRef](#)]
47. Sun, S.Z.; Liu, Z.; Dong, N. *Fluid Prediction for Paleokarst Carbonate Reservoir*; SEG Technical Program Expanded Abstracts; Society of Exploration Geophysicists: Houston, TX, USA, 2015; pp. 2821–2825.
48. Yang, X.; Wang, X.; Tang, H.; Ding, Y.; Lv, H.; Liu, C. The Early Hercynian Paleo-Karstification in the Block 12 of Tahe Oilfield, Northern Tarim Basin, China. *Carbonates Evaporites* **2014**, *29*, 251–261. [[CrossRef](#)]
49. Méndez, J.N.; Jin, Q.; González, M.; Zhang, X.; Lobo, C.; Boateng, C.D.; Zambrano, M. Fracture Characterization and Modeling of Karsted Carbonate Reservoirs: A Case Study in Tahe Oilfield, Tarim Basin (Western China). *Mar. Pet. Geol.* **2019**, *112*, 104104. [[CrossRef](#)]
50. Lin, B.; Zhang, X.; Xu, X.; Yuan, J.; Neng, Y.; Zhu, J. Features and effects of basement faults on deposition in the Tarim basin. *Earth-Sci. Rev.* **2015**, *145*, 43–55. [[CrossRef](#)]
51. Wang, Q.H.; Yang, H.J.; Li, Y.; Lü, X.; Zhang, Y.; Su, C.; Ouyang, S. Control of strike-slip fault on the large carbonate reservoir in Fuman, Tarim Basin a reservoir model. *Earth Sci. Front.* **2022**, *29*, 239–251.
52. Yun, L.; Deng, S. Structural styles of deep strike-slip faults in Tarim Basin and the characteristics of their control on reservoir formation and hydrocarbon accumulation: A case study of Shunbei oil and gas field. *Acta Pet. Sin.* **2022**, *42*, 770–787.

Disclaimer/Publisher's Note: The statements, opinions and data contained in all publications are solely those of the individual author(s) and contributor(s) and not of MDPI and/or the editor(s). MDPI and/or the editor(s) disclaim responsibility for any injury to people or property resulting from any ideas, methods, instructions or products referred to in the content.